Overview of Physics Results from MAST Upgrade Towards Core-Pedestal-Exhaust Integration

J. R. Harrison[1], A. Aboutaleb[2], S. Ahmed[3], M. Aljunid[1], S. Y. Allan[1], H. Anand[4], Y. Andrew[5], L. C. Appel[1], A. Ash[1], J. Ashton[1], O. Bachmann[1], M. Barnes[6], B. Barrett[1], D. Baver[7], D. Beckett[1], J. Bennett[1], J. Berkery[8], M. Bernert[9], W. Boeglin[2], C. Bowman[1], J. Bradley[10], D. Brida[9], P. K. Browning[11], D. Brunetti[1], P. Bryant[10], J. Bryant[10], J. Buchanan[1], N. Bulmer[1], A. Carruthers[1], M. Cecconello[12], Z. P. Chen[13], J. Clark[1,10], C. Cowley[14], M. Coy[1], N. Crocker[15], G. Cunningham[1], I. Cziegler[14], T. Da Assuncao[1], Y. Damizia[10], P. Davies[1], I. E. Day[1], G. L. Derks[16,17], S. Dixon[1], R. Doyle[18], M. Dreval[19], M. Dunne[9], B. P. Duval[20], T. Eagles[1], J. Edmond[1], H. El-Haroun[1], S. D. Elmore[1], Y. Enters[14], M. Faitsch[9], F. Federici[21], N. Fedorczak[22], F. Felici[20], A. R. Field[1], M. Fitzgerald[1], I. Fitzgerald[1], R. Fitzpatrick[13], L. Frassinetti[23], W. Fuller[24], D. Gahle[25], J. Galdon-Quiroga[26], L. Garzotti[1], S. Gee[1], T. Gheorghiu[14], S. Gibson[1], K. J. Gibson[14], C. Giroud[1], D. Greenhouse[14], V. H. Hall-Chen[27], C. J. Ham[1], R. Harrison[1], S. S. Henderson[1], C. Hickling[1,10], B. Hnat[24], L. Howlett[14], J. Hughes[28], R. Hussain[1], K. Imada[14], P. Jacquet[1], P. Jepson[1], B. Kandan[1], I. Katramados[1], Y. O. Kazakov[29], D. King[1], R. King[1], A. Kirk[1], M. Knolker[4], M. Kochan[1], L. Kogan[1], B. Kool[16,17], M. Kotschenreuther[13], M. Lees[1], A. W. Leonard[4], G. Liddiard[1], B. Lipschultz[14], Y. Q. Liu[4], B. A. Lomanowski[21], N. Lonigro[14], J. Lore[21], J. Lovell[21], S. Mahajan[13], F. Maiden[14], C. Man-Friel[1], F. Mansfield[1], S. Marsden[1], R. Martin[1], S. Mazzi[20], R. McAdams[1], G. McArdle[1], K. G. McClements[1], J. McClenaghan[4], D. McConville[1], K. McKay[10], C. McKnight[1], P. McKnight[1], A. McLean[30], B. F. McMillan[24], A. McShee[1], J. Measures[1], N. Mehay[1], C. A. Michael[15], F. Militello[1], D. Morbey[1], S. Mordijck[31], D. Moulton[1], O. Myatra[1], A. O. Nelson[32], M. Nicassio[1], M. G. O'Mullane[25], H. J. C. Oliver[1], P. Ollus[33], T. Osborne[4], N. Osborne[10], E. Parr[1], B. Parry[1], B. S. Patel[1], D. Payne[1], C. Paz-Soldan[32], A. Phelps[25], L. Piron[34,35], C. Piron[36], G. Prechel[37], M. Price[1], B. Pritchard[14], R. Proudfoot[1], H. Reimerdes[20], T. Rhodes[15], P. Richardson[1], J. Riquezes[32], J. F. Rivero-Rodriguez[1], C. M. Roach[1], M. Robson[1], K. Ronald[25], E. Rose[1], P. Ryan[1], D. Ryan[1], S. Saarelma[1], S. Sabbagh[32], R. Sarwar[1], P. Saunders[1], O. Sauter[20], R. Scannell[1], T. Schuett[14], R. Seath[1], R. Sharma[1], P. Shi[1], B. Sieglin[9], M. Simmonds[1], J. Smith[1], A. Smith[1], V. A. Soukhanovskii[30], D. Speirs[25], G. Staebler[4], R. Stephen[1], P. Stevenson[1], J. Stobbs[1], M. Stott[1], C. Stroud[1], C. Tame[1], C. Theiler[20], N. Thomas-Davies[1], A. J. Thornton[1], M. Tobin[32], M. Vallar[20], R. G. L. Vann[14], L. Velarde[38], K. Verhaegh[1], E. Viezzer[26], C. Vincent[1], G. Voss[1], M. Warr[1], W. Wehner[4], S. Wiesen[39], T. A. Wijkamp[16,17], D. Wilkins[1], T. Williams[1], T. Wilson[1], H. R. Wilson[14,21], H. Wong[15], M. Wood[1], V. Zamkovska[32]

[1] UKAEA (United Kingdom Atomic Energy Authority), Culham Science Centre, Abingdon, Oxfordshire, OX14 3DB, UK
[2] Department of Physics, Florida International University, 11200 SW, Miami, FL 33199, USA
[3] Department of Physics and Technology, UiT The Arctic University of Norway, N-9037 Tromsø, Norway
[4] General Atomics, PO Box 85608, San Diego, CA 92186-5608, USA

[5] Blackett Laboratory, Imperial College London - London, SW7 2BW, UK
[6] Rudolf Peierls Centre for Theoretical Physics, University of Oxford, Oxford OX1 3NP, UK
[7] Astrodel LLC, Boulder, Colorado 80303, USA
[8] Princeton Plasma Physics Laboratory, Princeton, NJ, USA
[9] Max-Planck-Institut fur Plasmaphysik, 85748 Garching, Germany
[10] Department of Electrical Engineering and Electronics, University of Liverpool, Brownlow Hill, Liverpool, L69 3GJ, UK
[11] Department of Physics and Astronomy, University of Manchester, Oxford Road, Manchester M13 9PL, UK
[12] Department of Physics, Durham University, Durham DH1 3LE, UK
[13] Institute for Fusion Studies, The University of Texas at Austin, Austin, TX, USA
[14] York Plasma Institute, Department of Physics, University of York, Heslington, York YO10 5DD, UK
[15] Physics and Astronomy Dept., University of California, Los Angeles, California 90098 USA
[16] Dutch Institute for Fundamental Energy Research DIFFER, Eindhoven, Netherlands
[17] Eindhoven University of Technology, Eindhoven, Netherlands
[18] Dublin City University, Dublin, Ireland
[19] National Science Center 'Kharkov Institute of Physics and Technology', Akademichna 1, Kharkiv 61108, Ukraine
[20] Ecole Polytechnique Fédérale de Lausanne (EPFL), Swiss Plasma Center (SPC), CH-1015 Lausanne, Switzerland
[21] Oak Ridge National Laboratory, Oak Ridge, Tennessee 37831, USA
[22] CEA, IRFM, F-13108 Saint-Paul-lez-Durance, France
[23] Division of Fusion Plasma Physics, KTH Royal Institute of Technology, Stockholm SE-100 44, Sweden
[24] Department of Physics, University of Warwick, Coventry, CV4 7AL, UK
[25] Department of Physics, SUPA, University of Strathclyde, Glasgow, Scotland, UK
[26] Dpto. de Física Atómica, Molecular y Nuclear, Universidad de Sevilla, 41012 Sevilla, España
[27] Institute of High Performance Computing, A*STAR, Singapore
[28] Plasma Science and Fusion Center, Massachusetts Institute of Technology, Cambridge, Massachusetts 02139, USA
[29] Laboratory for Plasma Physics, LPP-ERM/KMS, TEC Partner, Brussels, Belgium
[30] Lawrence Livermore National Laboratory, Livermore, CA, USA
[31] Dept. of Computer Science, College of William & Mary, Williamsburg, VA, USA
[32] Department of Applied Physics and Applied Mathematics, Columbia University, New York, NY, USA
[33] Department of Applied Physics, Aalto University, PO Box 11100, 00076 Aalto, Finland
[34] Dipartimento di Fisica "G. Galilei", Università degli Studi di Padova, Padova, Italy
[35] Consorzio RFX, Corso Stati Uniti 4, 35127, Padova, Italy
[36] ENEA, Fusion and Nuclear Safety Department, C. R. Frascati, Via E. Fermi 45, 00044, Frascati, Roma, Italy
[37] University of California Irvine, Irvine, CA 92697, USA
[38] Dpto. de Ingeniería Energética, ETSI, Universidad de Sevilla, 41092 Sevilla, España
[39] Forschungszentrum Jülich GmbH, Institut für Energie- und Klimaforschung—Plasmaphysik, 52425 Jülich, Germany

E-mail: James.Harrison@ukaea.uk

Received xxxxxx
Accepted for publication xxxxxx
Published xxxxxx

Abstract

Recent results from MAST Upgrade are presented, emphasising understanding the capabilities of this new device and deepening understanding of key physics issues for the operation of ITER and the design of future fusion power plants. The impact of MHD instabilities on fast ion confinement have been studied, including the first observation of fast ion losses correlated with Compressional and Global Alfvén Eigenmodes. High-performance plasma scenarios have ben developed by tailoring the early plasma current ramp phase to avoid internal reconnection events , resulting in a more monotonic q profile with low central

shear. The impact of m/n = 3/2, 2/1 and 1/1 modes on thermal plasma confinement and rotation profiles has been quantified, and scenarios optimised to avoid them have transiently reached values of normalised beta approaching 4.2. In pedestal and ELM physics, a maximum pedestal top temperature of ~350eV has been achieved, exceeding the value achieved on MAST at similar heating power. Mitigation of type-I ELMs with n=1 RMPs has been observed. Studies of plasma exhaust have concentrated on comparing conventional and Super-X divertor configurations, while X-point target, X-divertor and snowflake configurations have been developed and studied in parallel. In L-mode discharges, the separatrix density required to detach the outer divertors is approximately a factor 2 lower in the Super-X than the conventional configuration, in agreement with simulations. Detailed analysis of spectroscopy data from studies of the Super-X configuration reveal the importance of including plasma-molecule interactions and D_2 Fulcher band emission to properly quantify the rates of ionization, plasma-molecule interactions and volumetric recombination processes governing divertor detachment. In H-mode with conventional and Super-X configurations, the outer divertors are attached in the former and detached in the latter with no impact on core or pedestal confinement.

Keywords: term, term, term

1. Introduction and MAST Upgrade Capabilities

MAST Upgrade is a low aspect ratio tokamak (major radius (R) / minor radius (a) = 0.85/0.65 ~1.3, plasma current (I_p) ≤ 2.0 MA, toroidal field on axis (B_φ) ≤ 0.8 T, pulse length < 5 s) and one of the largest spherical tokamaks worldwide, together with NSTX-U [1]. It has considerable flexibility to independently vary the shape of the plasma core and divertors within tightly baffled chambers utilising 22 poloidal field coils to facilitate optimision of the shaping of the plasma core to maximise confinement and stability, whilst modifying the divertor configuration to maximise the dissipation of particles, momentum and energy. Sources of non-axisymmetic magnetic fields are available for ELM control with Resonant Magnetic Perturbations (RMPs) and correcting for intrinsic error fields, with two rows of in-vessel coils (four equally spaced toroidally above the mid-plane, eight below) and two pairs of ex-vessel coils respectively. On- and off-axis Neutral Beam Injectors (NBI) enable studies of the confinement of super Alfvénic fast ions that more closely mimics the products of fusion reactions. An extensive suite of highly resolved diagnostics is available to support a broad and deep physics programme in these key physics issues for the operation of ITER and the design of future power plants including DEMO [2] and STEP [3].

An optimal fine-alignment of the internal poloidal field coils to shape the plasma core and divertor was performed when assembling MAST-U to reduce the n=1 error field (EF) source associated with the coil design and manufacturing, which has foreseen coil shifts and tilts, of the order of mm and mrad, respectively [5]. To assess the presence of a residual n=1 EF, dedicated EF identification studies have been carried out and the main results are reported in Figure 1, which represents the compass scan tests executed in Ohmic scenarios with conventional divertor configurations at I_p = 450 kA, B_φ = 0.4 T and I_p = 750 kA, B_φ = 0.5 T. In both scenarios, EF identification studies suggest that a homeopathic level of correction currents are needed to minimise the intrinsic EF amplitude, of around some hundreds of A. This suggests that the intrinsic EF amplitude is smaller than in MAST, where the EF correction currents were in the kilo Ampere regime [6]. This proves that the coil alignment when assembling the device so as to minimise the intrinsic n=1 EF has been a successful passive n=1 EF correction strategy.

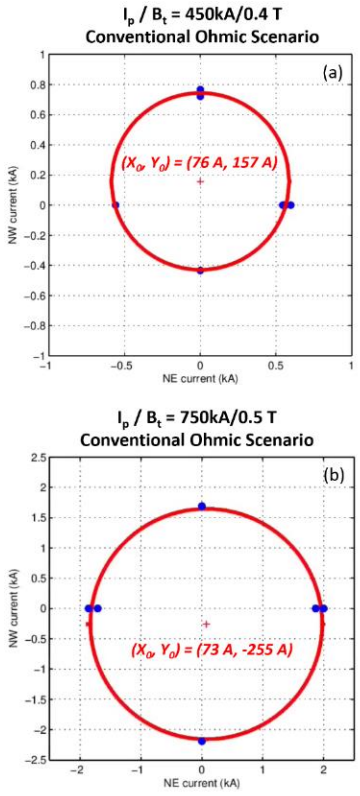

Figure 1: Quantification of the intrinsic error field in Ip = a) 450 kA and (b) 750 kA plasma scenarios using the compass scan technique [4].

Recent results from MAST Upgrade are presented, including fast particle physics in section 2, MHD stability and maximising beta in section 3, pedestal and Edge Localised Mode (ELM) physics in section 4, plasma exhaust with an emphasis on the relative benefits of alternative divertor configurations in section 5 and plasma control and the development of high-performance plasma scenarios in section 6. A programme of extensive hardware enhancements is underway to further develop the capabilities of MAST Upgrade. These enhancements and the envisaged future MAST Upgrade programme are presented in section 7.

2. Fast Particle Physics

Future large burning fusion devices with a significant α particle population will require good confinement of charged fusion products to maximise plasma self-heating and minimising heat fluxes arising from losses. MAST Upgrade is well suited to studying fast particle confinement and the impact of MHD instabilities, with on-and off-axis neutral beams (with tangency positions (R, Z) of (0.71 m, 0.0 m) and (0.8 m, 0.65 m) respectively) that produce anisotropic super-Alfvénic fast ions (for example, in a typical pulse the speed of the deposited fast ions v_{fi} ~2.5×10^6 m/s exceeds the Alfvén speed in the core v_A ~1.5×10^6 m/s [7]). A comprehensive suite of highly resolved diagnostics is available, including a fission chamber [8], upgraded neutron camera [7], Solid State Neutral Particle Analyser (SSNPA) [9], Fast Ion Loss Detector (FILD) [10] and a Fast-Ion Deuterium Alpha (FIDA) system [11]. Despite the closed divertors reducing the neutral density in the main chamber, inferred from mid-plane radial profiles of n_e, T_e and D_α emission, up to 20% of the injected NBI power from both beams are lost due to charge-exchange interactions with edge neutrals [12], and including these interactions enables reconstruction of the passive FIDA signal.

A broad spectrum of fast ion driven instabilities are excited including toroidal (TAE), compressional (CAE) and global (GAE) Alfvén eigenmodes, fishbones, as shown in *Figure 2*, mostly due to fast ions produced by the on-axis beam. The impact of these instabilities on the thermal plasma and fast ion confinement has been studied in detail. The largest source of fast ion losses is 2/1 tearing modes that are commonly observed in NBI heated pulses (see Section 3). The tearing mode amplitude typically grows throughout the NBI heated phase of a pulse that can reduce the measured neutron rate by up to 50%. Significant changes in the fast ion population are observed following sawtooth crashes [7], that can reduce the fast ion population by 40-50% across the plasma core, in agreement with similar findings on MAST [13]. Fast ion losses in the core due to fishbones have been observed with neutron camera and FILD diagnostics, that can reduce the fast ion density by ~20%, up to 35% near the magnetic axis, indicating a hollow neutron profile as the fishbone grows, then in the later phase becomes peaked in the core slightly toward the inboard side. Interpretive modelling with ASCOT and FILD measurements suggest these losses are of trapped fast ions [14]. Conversely, TAEs are correlated with fast ion losses only when the off-axis neutral beam is applied, otherwise they tend to result in fast ion redistribution.

For the first time, FILD measurements indicate that CAEs and GAEs have been correlated with fast ion losses. The location of these modes has been determined with Doppler backscattering (DBS) measurements, finding that modes that are more localised to the plasma core (up to $\sqrt{\psi_N}$~0.7) result in fast ion redistribution, whereas modes localised near the edge (up to $\sqrt{\psi_N}$~0.9) result in fast ion losses. Conversely, TAEs are found to result in fast ion redistribution. Evidence for ion cyclotron emission from Ohmic plasmas has been observed in density fluctuations measured by DBS with a frequency of ~3.5 MHz [16].

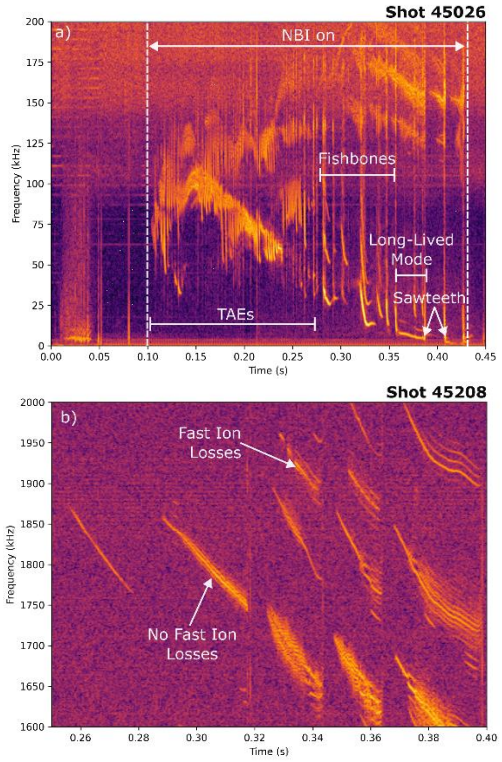

Figure 2: Spectrograms of magnetic fluctuations a) illustrating commonly observed fast particle driven instabilities, including chirping/bursting TAEs, n=1 internal kink modes (chirping fishbones then long-lived mode) and sawteeth (based on [15]) and b) CAE/GAE modes and whether they correlate with fast ion losses, measured with a Fast Ion Loss Detector.

Fast ion redistribution and losses due to ELMs have been measured with the FILD, SSNPA and FIDA diagnostics. Type-III ELMs are observed to have minimal impact on global fast ion confinement as the neutron rate is not strongly affected [17]. However, these ELMs result in localised fast ion losses, likely from the plasma edge, with no fast-ion acceleration correlated with ELMs. Fast ion losses due to the presence of resonant magnetic perturbations have also been observed.

3. Core MHD Stability and Maximising Beta

The avoidance of performance limiting and disruptive MHD instabilities is highly desirable to maximise fusion performance and reduce the risk of damage to the interior surfaces of a fusion device respectively. Therefore, identification and avoidance of these instabilities is a key objective of the MAST Upgrade programme. Typical plasma scenarios have a rapid initial plasma current ramp rate, dI_p/dt ~6.5MA/s, prior to the flat-top phase and Internal Reconnection Events (IREs) are common. IREs are observed to cause a transient increase in plasma current (I_p) and loop voltage, and reduction in plasma density, resulting in current redistribution from a hollow, reverse shear q profile to a broad, monotonic one [18]. IREs have been successfully avoided with slower I_p ramp rates, ~3.5 MA/s, resulting in more monotonic q profiles with lower central shear.

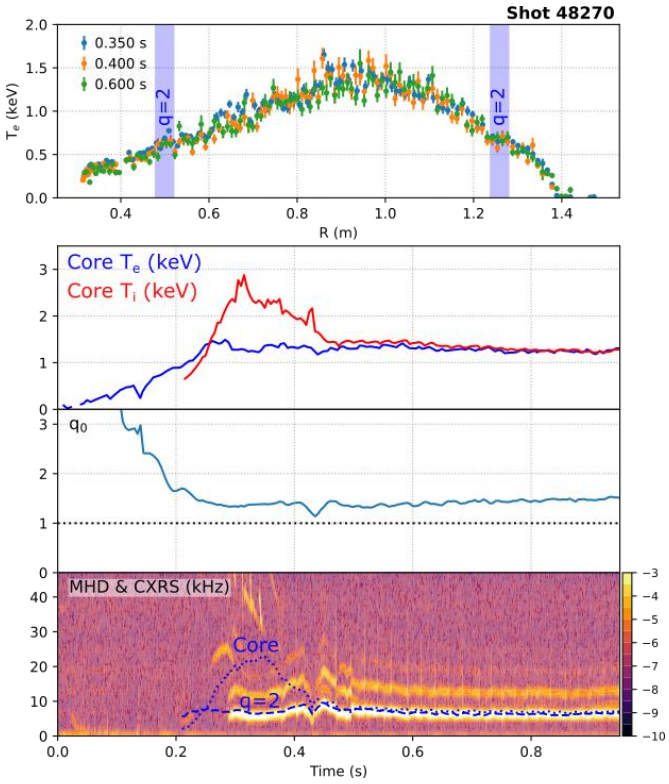

Figure 3: Overview of a typical pulse with a performance limiting tearing mode. Top: Thomson scattering profiles of T_e showing flattening at the q=2 surface, middle: core T_e, T_i, bottom: spectrogram of low frequency magnetic fluctuations with the toroidal rotation at the magnetic axis and q = 2 flux surface.

The performance of MAST Upgrade plasmas with strong auxiliary heating is typically moderated by m/n = 1/1, 2/1 and 3/2 modes, which dampen the rotation profile (the higher order modes mostly reduce the core rotation, whereas the lower order modes reduce the entire rotation profile) and reduce core confinement. The 1/1 mode is qualitatively similar to the long-lived mode studied on MAST [19], except that it does not always limit the pulse duration and higher order harmonics are weaker in spectrograms of magnetic field fluctuations. The 2/1 tearing mode causes a characteristic frequency of 6-10 kHz and causes flattening of the T_e profile at the q=2 flux surface. The rotation frequency of the mode is consistent with plasma rotation profile measurements at the q=2 surface, as shown in *Figure 3*. To avoid these instabilities, the initial I_p current ramp has been optimised to avoid the IRE. The slower I_p current ramp tends to reduce q_0 in the early Ip flat-top phase, while the off-axis neutral beam provides additional current drive to help elevate q_0. Further plasma scenario optimisations are underway to vary I_p, B_φ and elongation (κ) to maximise normalised beta (β_N), then other metrics. The off-axis neutral beam is an effective source of non-inductive current drive that allows $q_0 > 1$ to be sustained throughout a pulse, as shown in *Figure 3*, thus avoiding sawteeth. To date, the highest achieved β_N is ~4.2 transiently in shot 48653, which reached a maximum stored energy of ~160 kJ prior to the locking of 2/1 and 1/1 modes that resulted in a disruption. These results built on work carried out in previous campaigns where β_N was limited to ~3 by non-disruptive mode locking events [20]. In support of further optimising plasma performance, the highest achievable elongation for a given ℓ_i has been characterised. To date, κ up to 2.4 has been achieved with good vertical control.

Density limits have been studied [21], finding that disruptivity increases with proximity to the Greenwald density limit [22]. Of the few density limit disruptions observed to date, they cross a threshold based on the turbulent transport for a given heating power across the separatrix [23]. Investigation of disruption causes (indicated by abnormalities in the plasma current and vertical position development) with the DECAF™ [24] code revealed a year-to-year (in the first and second physics campaigns) decrease by ~ 20% of the plasma disruptivity rate. These improvements in scenario robustness were enabled through better real-time control of the plasma shape and density. Trigger instances of disruptive event chains were clustered in different parts of the operation space

diagrams and plasma elongation was shown to be an important factor influencing details of the chains [25].

4. Pedestal and ELM Physics

MAST Upgrade routinely operates in the high confinement mode (H-mode), with auxiliary heating from the on- and off-axis neutral beams. Initial studies on H-mode access have concentrated on the impact of the divertor configuration on P_{L-H}, indicating broadly similar values for conventional and Super-X divertor configurations.

In H-mode, radial profiles of electron density (n_e) and temperature (T_e) at the edge of the confined plasma exhibit steep gradients emblematic of the edge pedestal. The density and temperature pedestal characteristics were diagnosed with a high-resolution Thomson scattering system in MAST [26] and MAST Upgrade, where the pedestal top parameters are shown in *Figure 4*. There is significant overlap in the achieved pedestal top parameters in both devices, however MAST Upgrade is able to sustain hotter pedestals where $T_{e,ped}$ > 350eV, which was not possible in MAST with comparable auxiliary heating power. The transition from type-III to type-I ELMs is observed to occur when the power crossing the separatrix is ~1.9 MW and $T_{e,ped}$ ~130 eV [27], which is lower than comparable values on MAST of ~2.5 MW and 150 eV respectively [28].

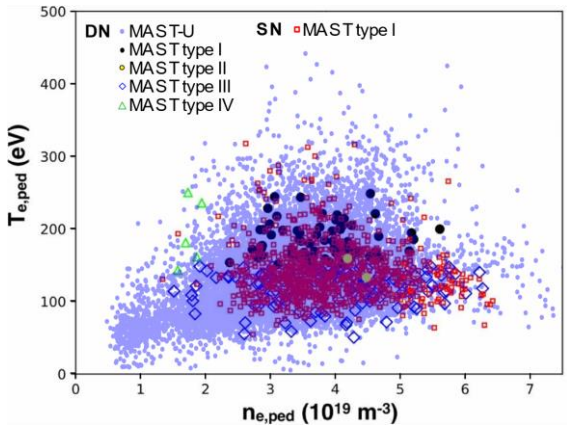

Figure 4: Electron density and temperature pedestal height in MAST [26] in double null (DN) and single null (SN) topologies and MAST Upgrade.

The MHD and gyrokinetic stability of MAST pedestals was analysed with the ELITE and CGYRO codes [29], showing that the pedestal was constrained by kinetic ballooning and medium toroidal mode number peeling-ballooning modes. Stability analysis of MAST Upgrade pedestals [30], shown in *Figure 5*, indicates that the higher elongation and squareness of the plasma boundary, compared with MAST, due to improved plasma shaping, enabled by the larger number of poloidal field coils and higher toroidal field in MAST Upgrade and enables operation at higher normalised pedestal pressure, closer to the peeling boundary. This analysis suggests that the squareness of the plasma boundary is close to optimal, but further improvements in pedestal stability, and in turn the pedestal pressure, are possible by increasing elongation and maximising particle pumping and auxiliary heating power available in upcoming improvements to the device to reduce the pedestal collisionality.

Mitigation of type-I ELMs with Resonant Magnetic Perturbations (RMPs) with toroidal mode number, n = 1 has been achieved. The application of n = 1 RMPs leads to an increase in the ELM frequency and deceleration and locking of a 2/1 tearing mode that is common to typical type-I ELMy H-mode scenarios (as discussed in Section 3) and then density pump-out. Removal of the RMPs results in the mode rotation accelerating and the ELM frequency decreasing to their original values.

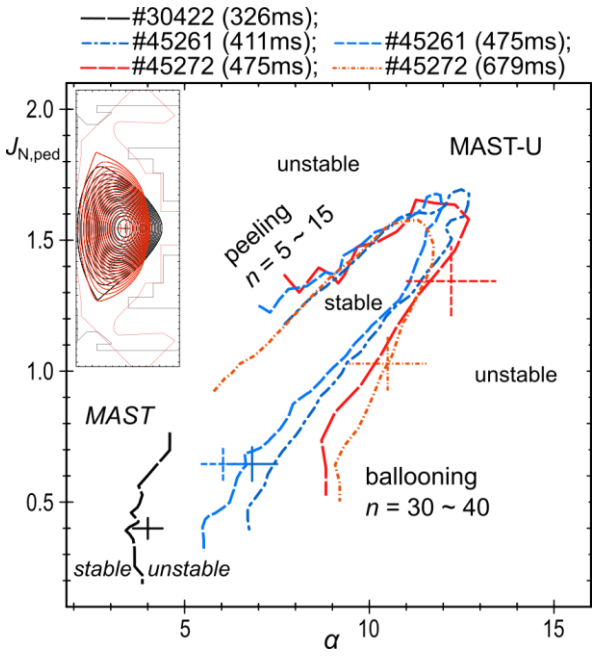

Figure 5: Pedestal stability boundaries in terms of normalised pedestal pressure gradient on the x-axis and current density on the y-axis on MAST (black) and MAST-U (blue, red). The inset figure shows MAST (black) and MAST-U (red) equilibria analysed.

5. Plasma Exhaust and Alternative Divertor Configurations

MAST Upgrade has significant flexibility to develop and study conventional and alternative divertor configurations, with and without up-down symmetry, including the X-divertor [31, 32], Super-X [33], Snowflake [34] and X-point target [35], as shown in *Figure 6*. The early MAST Upgrade programme prioritised comparing the Super-X with a conventional divertor configuration, including the role of total flux expansion tightly baffled divertor chambers on plasma exhaust. In spherical tokamaks, the benefits of the Super-X configuration are amplified, such as higher total flux expansion (~2.5 in MAST-U, compared with < 1.7 in TCV [36]), and consequently strong gradients in the total magnetic field from the X-point to the divertor target that is predicted to passively stabilise the movement of the detachment front [37]. Consequently, an extensive suite of diagnostics was deployed and optimised to study the Super-X divertor configuration, including 850 Langmuir probes [38], a divertor Thomson scattering system [39], a multi-wavelength imaging system [40], resistive [41] and imaging [42] bolometer diagnostics, UV-visible spectrometers, neutral pressure gauges and IR thermography. Other divertor configurations are being developed and studied in parallel, particularly the snowflake [43] and X-point target.

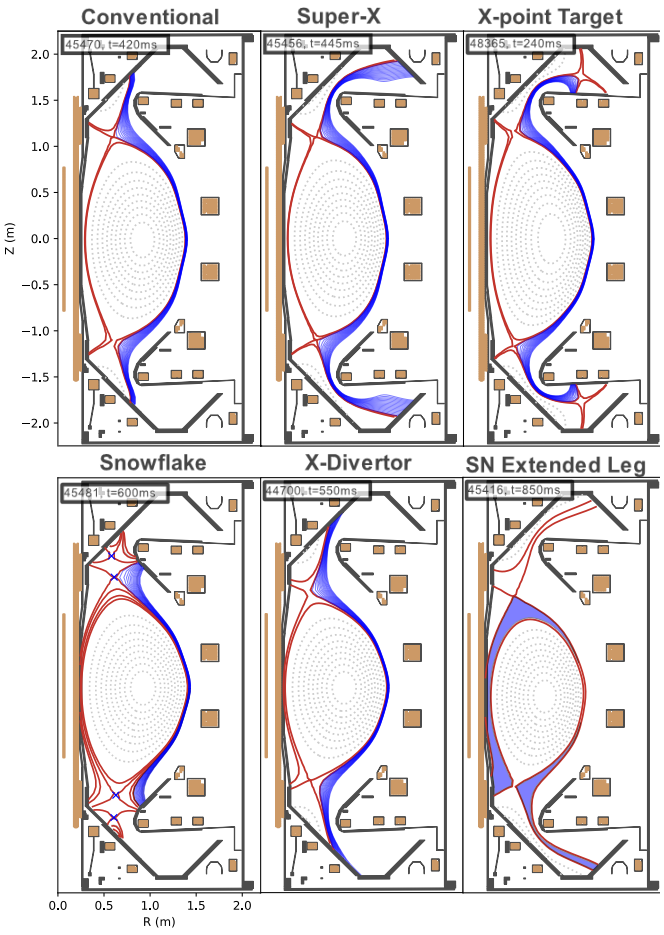

Figure 6: Equilibrium reconstructions of conventional and alternative divertor configurations developed on MAST-U.

Initial comparisons of conventional and Super-X divertor configurations were performed in Ohmic and NBI heated L-mode pulses. Experiments were performed with density ramps and repeat pulses at different (constant) flat-top density to quantify the onset of divertor detachment. The detachment threshold, in terms of the estimated separatrix density, was a factor of two lower in the Super-X configuration than a conventional divertor, as shown in Figure *7*, in broad agreement with predictions from analytic models (e.g. [37]). The divertor surface power load was reduced by at least an order of magnitude in the Super-X configuration. The mid-plane n_e and T_e profiles at a given line-average density were not significantly affected by either the divertor configuration

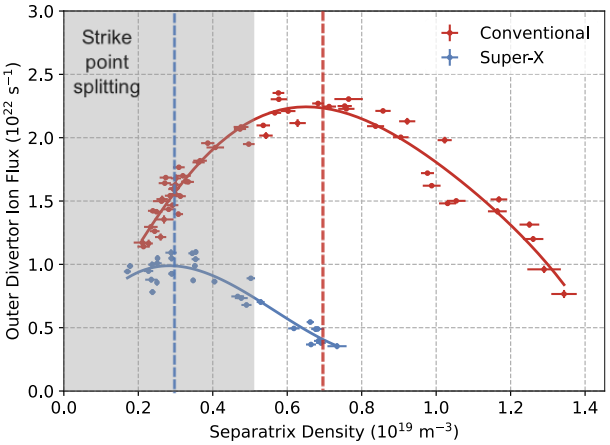

Figure 7: Measured total divertor ion flux in conventional (red) and Super-X (blue) divertor configurations. Estimated detachment thresholds are given by vertical dashed lines.

or whether the outer divertors were detached. This detachment behaviour in the Super-X divertor configuration is well reproduced in predictive [44] and interpretive SOLPS-ITER simulations [45], however the simulations of the conventional configuration do not exhibit the characteristic roll-over in the total divertor ion flux, which is thought to be due to a reduction in the upstream separatrix pressure in experiments from strong power losses originating from the strong gas fuelling applied to reach the required core line-average density.

Multi-wavelength imaging of the D_2 Fulcher band emission from the lower divertor chamber was used to estimate the position of the ionization front, where the dominant form of plasma-neutral interactions transitions from electron impact ionisation to plasma-molecule interactions [46]. As the plasma conditions in the divertor chambers trend toward deeper detachment, the ionisation front moves from the outer strike point towards the divertor entrance. The observed sensitivity of the ionisation front movement with increasing mid-plane separatrix density agrees well with interpretive

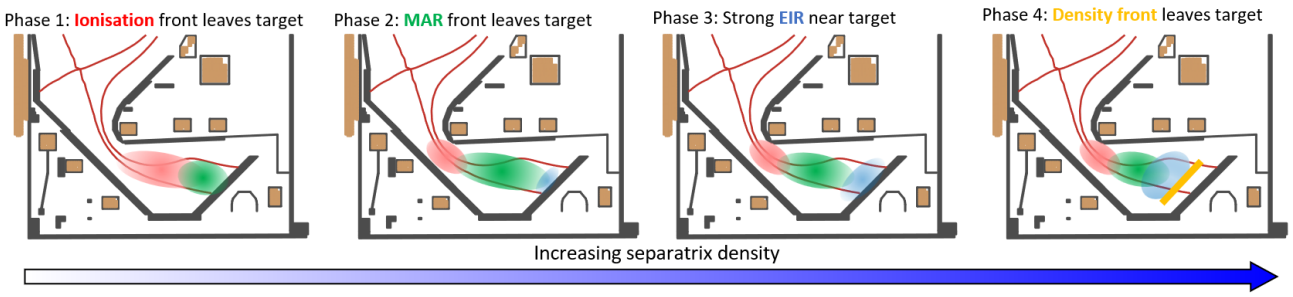

Figure 9: Phases of divertor detachment observed in spectroscopic studies of the lower divertor chamber

SOLPS-ITER simulations [47]. There is a clear reduction in the sensitivity of the front position to changes in the separatrix density as the emission front moves through regions exhibiting strong gradients in the total magnetic field, in agreement with analytic models [37, 48].

Studies of NBI heated L-mode pulses with conventional, Super-X and an intermediate, elongated, divertor configuration elucidate the benefits of increased divertor volume on power and particle exhaust [49]. In the elongated and Super-X divertor configurations after the onset of detachment, the ionisation region in the divertor chamber extends to a fixed major radius, insensitive to increases in the major radius of the outer strike points. Downstream of the ionisation region, any additional divertor volume afforded by a larger outer strike point major radius increases ion sinks, including molecular activated recombination and electron-ion recombination, and power losses due to plasma-neutral interactions that reduce divertor target power and particle fluxes.

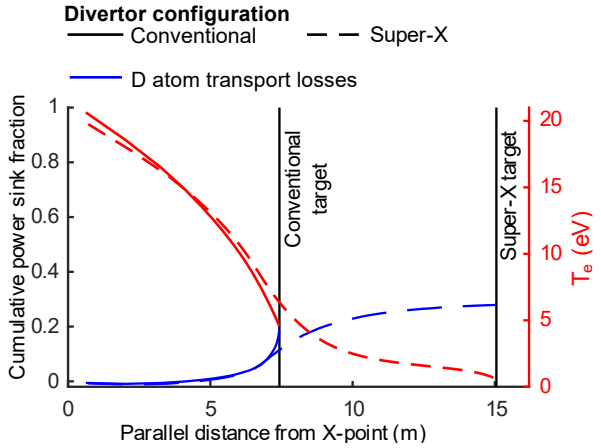

Figure 8: Profiles of the electron temperature (red) and power losses due to plasma-atom interactions (blue) along the separatrix flux surface from the divertor entrance to the target in conventional and Super-X divertor configurations simulated with SOLPS-ITER.

Experiments performed in type-I ELMy H-mode scenarios with conventional and Super-X divertor configurations and similar core shaping are in broad agreement with the L-mode studies. In 750 kA scenarios, which maximise the ratio of the separatrix density at the midplane and the parallel heat flux entering the divertor chambers to ease access to attached divertor conditions, with ~3 MW of NBI heating power, the conventional divertor configuration was attached and the Super-X detached. In common with L-mode experiments, global confinement parameters, including $H_{IPB98y,2}$ and β, and core and pedestal n_e and T_e profiles were also unaffected by whether the divertor was in a conventional or Super-X configuration and whether the outer divertors are attached or detached. These observations are in good qualitative agreement with SOLPS-ITER simulations, shown in *Figure 8*, that the plasma conditions in conventional and Super-X configurations are similar for otherwise similar boundary conditions, but T_e at the divertor entrance is lower in the Super-X configuration due to higher power losses due to plasma-neutral interactions in the additional divertor volume where $T_e < 5$ eV. The divertor neutral compression, the ratio of the lower divertor and main chamber neutral pressures, is typically 100-300, with the Super-X having higher compression despite the outer divertors being detached.

The fundamental mechanisms governing detachment in the Super-X divertor configuration have been studied in experiments via spectroscopic measurements interpreted using a sophisticated Bayesian framework BaSPMI [46]. To correctly interpret these measurements, it is necessary to account for plasma-molecule interactions and measurements of the D_2 Fulcher band emission profile are needed to discern between emission due to electron impact excitation, which in turn can be used to estimate where ionisation of neutrals occurs, and plasma-molecule interactions. In Ohmic and NBI heated L-mode pulses, 4 distinct detachment phases were observed, as shown in Figure 9. At detachment onset, in phase 1, the ionisation front, inferred from the trailing edge of D_2 Fulcher band emission, pulls away from the divertor target, with evidence of Molecular Activated Recombination (MAR) occurring downstream. In phase 2, the region where MAR interactions occur pulls away from the target and the outer

divertor particle flux reduces with increasing fuelling, there is evidence of Electron-Ion Recombination (EIR) occurring downstream, suggestive that the target electron temperature $T_{e,t}$ ~0.8 eV. In phase 3, the frequency of EIR interactions increases and $T_{e,t}$ ~ 0.5 eV . In phase 4, normally prior to a density limit disruption, all 3 emission regions move toward the divertor entrance and the peak in the divertor electron density pulls away from the target and $T_{e,t} << 0.5$ eV. Due to T_e being low across the outer divertor leg in the Super-X configuration, radiation from carbon is thought to have a negligible contribution to power dissipation in the divertor chambers. Moreover, the low temperature in the divertor results explains why EIR in the divertor is prevalent, despite the density being modest (~1-3x10^{19} m^{-3}) and SOLPS-ITER simulations being more susceptible to inaccuracies in the rates of atomic and molecular processes, in particular of molecular charge-exchange [50, 51]. Radiation trapping from deuterium and carbon are predicted to be small, based on predictive simulations with the CRETIN code [52].

6. Plasma Control and Development of High-Performance Scenarios

The MAST Upgrade Plasma Control System (PCS) is based on the framework developed at General Atomics [53] with improvements to accommodate the larger number of gas injection locations and coil current control [54]. Real-time sensing of the inner and outer radii of the Last Closed Flux Surface (LCFS) at the mid-plane, radial and vertical position of the lower X-point and the position of the lower outer divertor strike point is provided by LEMUR [55], a local higher order expansion of poloidal flux, fitted to magnetic field and flux measurements and constrained by the Grad-Shafranov equation in the vacuum region. Prior to deployment on MAST-U, LEMUR was successfully validated against experiments on DIII-D [56]. Real-time manipulation of the plasma shape parameters sensed by LEMUR, and feedforward control of other parameters (e.g. squareness of the LCFS, poloidal flux expansion at the outer divertor, etc) independently is facilitated by linear shape control "virtual circuits" that map changes to individual plasma shape parameters, whilst keeping the others of interest fixed, to changes in poloidal field coil currents [57]. Control of the plasma density is facilitated by real-time measurements of the line-integrated density using an interferometer chord at the mid-plane [58] and an arbitrary combination of gas valves. Detachment control has been successfully demonstrated using multi-wavelength imaging to estimate the position of the ionisation front in the lower divertor chamber, as discussed in Section 5, and gas fuelling from the main chamber was used to vary the detachment state.

Plasma scenarios have been developed at Ip = 450, 600, 750, 1000 kA, mostly with either conventional or Super-X divertor configurations. Plasma breakdown is performed via direct induction and a hot filament provides a source of free electrons. The initial loop voltage and pre-fill gas pressure have been optimised to minimise solenoid flux consumption and is robust to changes in vessel conditions, such as after boronizations. In the I_p ramp-up phase, the plasma volume, outer radius and elongation expand rapidly to slow current penetration to the magnetic axis, thus maximising q_0 and minimising ℓ_i. This is favourable for sustaining strong shaping of the plasma boundary, in particular high elongation, and to avoid the onset of low order performance-limiting instabilities such as the long-lived mode [19], but would increase the likelihood of reverse magnetic shear which is destabilising for helical core type modes.

The development of high-performance scenarios has two elements, concentrating on increasing I_p, to increase confinement of the thermal and fast particle populations and maximising β at intermediate I_p, as discussed in Section 3. The 750 kA scenarios are the most widely used to date, benefitting from satisfactory confinement for the majority of the scientific programme and can be executed with Ohmic heating only or with NBI with sufficiently long I_p flat-top duration. Therefore, these scenarios are the most mature and thoroughly studied. To develop a robust H-mode scenario, the gap between the inner wall and the LCFS is at least 3cm, the vertical position is optimised to maintain a connected double null topology and only fuelling from the high-field side is used, all of which promote H-mode access. With these optimisations applied, maximum core electron and ion temperatures of 2 keV and 3 keV respectively with energy confinement normalised to the ITER scaling [59] $H_{IPB98y,2}$ ~1.3 have been achieved. As discussed in Section 3, the performance of these scenarios is typically limited by 2/1 tearing modes, which tends to reduce the energy confinement to $H_{IPB98y,2}$ ~1. The mode amplitude is moderated, and its rotation frequency maintained, via a combination of off-axis neutral beam injection, moderate gas fuelling after the L-H transition and reducing β and κ [27].

The development of higher I_p scenarios is underway and exhibits similar performance limiting MHD and shares common amelioration strategies with the 750 kA scenarios. To date, a 1000 kA scenario with a conventional divertor has reached 500 ms duration. Further optimisations of this scenario, through careful tailoring of gas fuelling, elongation, timings of NBI injection and toroidal field are expected to improve scenario performance and pulse duration further.

7. Hardware Enhancements and Future Programme

A phased programme of enhancements to the heating, fuelling and pumping capabilities of MAST Upgrade are underway to access more reactor-relevant plasma conditions, including lower collisionality in the core, pedestal and divertor, higher divertor heat flux, maximum divertor neutral pressure and higher beta for longer pulses. By the end of 2023, a divertor cryopump will be operational to provide a tenfold increase in particle pumping to significantly improve particle control for longer pulse operations and is predicted to expand the range of operating parameters where attached divertor operation is possible [60]. In 2024, a 1.6 MW electron Bernstein wave heating and current drive system with injection frequencies of 28 GHz and 34.8GHz will enable studies of on-and off-axis heating and current drive in the plasma current ramp-up and flat-top phases. In 2025, two additional neutral beam injectors will be installed, increasing the maximum injected power by up to 2.5 MW of off-axis heating and 2.5 MW intermediate between the on-axis and off-axis injectors, to double the total neutral beam heating power to a maximum of 10 MW and to further tailor the fast ion pressure profile for the avoidance of energetic particle modes. In parallel, a high frequency pellet injector will be commissioned to study the impact of reactor-relevant fuelling on scenario performance and control, emphasising studies to optimise core and pedestal confinement with acceptable power exhaust in the presence of transient particle fluxes.

These new capabilities will facilitate deep physics studies into key physics issues for future tokamaks, including non-inductive current drive with electron Bernstein waves, fast particle physics with fine control of the fast ion pressure profile, studies of core and pedestal confinement and MHD stability at higher performance and their integration with highly dissipative alternative divertor configurations. Future physics programmes will aim to advance understanding in these areas in parallel as the capabilities of the device improves. It is envisaged that studies of power and particle exhaust will advance to study detachment induced via impurity seeding and understanding the controllability of divertor detachment in a wider variety of divertor configurations, including the X-point target, X divertor and snowflake and their response to transients arising from pellet injection and MHD, including ELMs. The development and study of stationary high-performance regimes will have greater emphasis in future campaigns, as the lower pedestal collisionality afforded by the higher heating power and pumping speed is expected to facilitate access to naturally ELM-free pedestal regimes such as the QH-mode. In parallel, the programme of experiments will be accompanied by modelling predictions to test predictive tools and deepen our understanding of experiments.

Acknowledgements

This work has been carried out within the framework of the EUROfusion Consortium, funded by the European Union via the Euratom Research and Training Programme (Grant Agreement No 101052200 — EUROfusion) and from the EPSRC [grant numbers EP/W006839/1 and EP/T012250/1]. To obtain further information on the data and models underlying this paper please contact PublicationsManager@ukaea.uk. Views and opinions expressed are however those of the author(s) only and do not necessarily reflect those of the European Union or the European Commission. Neither the European Union nor the European Commission can be held responsible for them.

References

[1] J. E. Menard et al,. Nucl. Fusion **57** 102006 (2017)
[2] G. Federici et al., Nucl. Fusion **59** 066013 (2019)
[3] H. R. Wilson et al., Commercialising Fusion Energy 2053-2563 (Bristol: IOP Publishing) 81
[4] T.C. Hender et al Nucl. Fusion **32** 2091 (1992)
[5] L. Piron et al., Fusion Eng. and Design **161** 111932 (2020)
[6] A. Kirk at al., Plasma Phys. Control. Fusion **56** 104003 (2014)
[7] M. Cecconello et al., Plasma Phys. Control. Fusion **65** 035013 (2023)
[8] C. Vincent et al., Rev. Sci. Instrum. **93** 093509 (2022)
[9] G. Prechel et al., Rev. Sci. Instrum. **93** 113517 (2022)
[10] J. F. Rivero-Rodriguez et al., Rev. Sci. Instrum. **89** 10I112 (2018)
[11] C A Michael et al., Plasma Phys. Control. Fusion **55** 095007 (2013)
[12] P. Ollus et al., (in press) Plasma. Phys. Control. Fusion (2023)
[13] M. Cecconello, A. Sperduti, Plasma Phys. Control. Fusion **60** 055008 (2018)
[14] J. F. Rivero-Rodriguez et al., ECPD 2023
[15] A. Jackson, Proc. 49th EPS Conf. on Plasma Physics (2023)
[16] T. L. Rhodes et al., Rev. Sci. Instrum. **93** 113549 (2022)
[17] L. Velarde et al., Proc. 49th EPS Conf. on Plasma Physics (2023)
[18] S. Gibson et al., 48th European Physical Society Conf. on Plasma Physics (2023)
[19] I. T. Chapman et al., Nucl. Fusion **50** 045007 (2010)
[20] J. W. Berkery et al., Plasma Phys. Control. Fusion **65** 045001 (2023)
[21] J. W. Berkery et al., Plasma Phys. Control. Fusion **65** 095003 (2023)
[22] M. Greenwald et al., Nucl. Fusion **28** 2199 (1988)
[23] M. Giacomin et al., Phys. Rev. Lett. **128** 185003 (2022)
[24] S.A. Sabbagh et al., Physics of Plasmas **30** 111945 (2023)

[25] V. Zamkovska et al., Proc. 29th IAEA Int. Conf. in Fusion Energy (2023)
[26] S. F. Smith et al., Plasma Phys. Control. Fusion **64** 045024 (2022)
[27] A. J. Thornton et al., Proc. 29th IAEA Int. Conf. in Fusion Energy (2023)
[28] A. Kirk et al., Plasma Phys. Control. Fusion **51** 065016 (2009)
[29] M. Knolker et al., Nucl. Fusion **61** 046041 (2021)
[30] K. Imada et al,. in prep
[31] H. Takase, J. Phys. Soc. Japan **70** 609 (2001)
[32] M. Kotschenreuther, P. M. Valanju, S. M. Mahajan, J. C. Wiley, Phys. Plasmas **14** 072502 (2007)
[33] P. M. Valanju, M. Kotschenreuther, S. M. Mahajan, J. Canik, Phys. Plasmas **16** 056110 (2009)
[34] D. D. Ryutov Phys. Plasmas **14** 064502 (2007)
[35] B. LaBombard et al., Nucl. Fusion **55** 053020 (2015)
[36] C. Theiler et al., Nucl. Fusion **57** 072008 (2017)
[37] B. Lipschultz et al., Nucl. Fusion **56** 056007 (2016)
[38] P. Ryan et al., subm. Rev. Sci. Instrum
[39] J. G. Clark et al., Rev. Sci. Instrum. **93**, 103534 (2022)
[40] X. Feng et al., Rev Sci Instrum **92**, 063510 (2021)
[41] J. Lovell et al., Rev Sci Instrum **94**, 023509 (2023)
[42] F. Federici et al., Rev Sci Instrum **94**, 033502 (2023)
[43] V. A. Soukhanovskii et al., Nucl. Mater. Energy **33** 101278 (2022)
[44] A. Fil et al., Nucl. Fusion **62** 096026 (2022)
[45] D. Moulton et al., Proc. 29th IAEA Int. Conf. in Fusion Energy (2023)
[46] K. Verhaegh et al., Nucl. Fusion **63** 016014 (2023)
[47] O. Myatra et al., Nucl.Fusion **63** 096018 (2023)
[48] C. Cowley et al., Nucl. Fus. **62** 086046 (2022)
[49] K. Verhaegh et al., Proc. 29th IAEA Int. Conf. in Fusion Energy (2023)
[50] K. Verhaegh et al., Nucl. Fusion **63** 076015 (2023)
[51] O. Myatra et al., Nucl. Fusion **63** 076030 (2023)
[52] V. A. Soukhanovskii et al., Nucl. Fusion **62** 066047 (2022)
[53] B. G. Penaflor. Proc. 19th Symposium on Fusion Technology 965-968 (1996)
[54] G. McArdle et al., Fusion Eng. Des. **159** 111764 (2020)
[55] M. Kochan et al., 30th IEEE Symosium on Fusion Engineering, (2023).
[56] H. Anand et al., Fusion Eng. Des. **177** 113086 (2022)
[57] H. Anand et al., Proc. 29th IAEA Int. Conf. in Fusion Energy (2023)
[58] T. O'Gorman et al., Rev. Sci. Instrum. **85** 11D861 (2014)
[59] O. Kardaun, Plasma Phys. Control. Fusion **41** 429 (1999)
[60] E. Havlíčková et al., Plasma Phys. Control. Fusion **57** 115001 (2015)